Appl. Phys. B 88, 273–279 (2007)
DOI: 10.1007/s00340-007-2673-z

Applied Physics B
Lasers and Optics

W. WANG[1,2]
P.X. WANG[1,✉]
Y.K. HO[1]
Q. KONG[1]
Y. GU[2]
S.J. WANG[2]

Effects of sidelobes of focused flat-topped laser beams on vacuum electron acceleration

[1] Applied Ion Beam Physics Laboratory, Key Laboratory of the Ministry of Education, Institute of Modern Physics, Fudan University, Shanghai 200433, P.R. China
[2] Shanghai Institute of Laser Plasma, Shanghai 201800, P.R. China

Received: 4 December 2006/Revised version: 20 April 2007
Published online: 13 June 2007 •

ABSTRACT Using three-dimensional test particle simulations, we investigated electrons accelerated by a focused flat-top laser beam at different intensities and flatness levels of the beam profile before focusing in vacuum. The results show that the presence of sidelobes around the main focal spot of the focused flat-top laser beam influences the optimum (as far as electron acceleration is concerned) initial momentum (and incident angle) of electrons for acceleration. The difference of initial conditions between laser beams with and without sidelobes becomes evident when the laser field is strong enough ($a_0 > 10$, corresponding to intensities $I > 1 \times 10^{20}\,\mathrm{W/cm^2}$ for the laser wavelength $\lambda = 1\,\mu\mathrm{m}$, where a_0 is a dimensionless parameter measuring laser intensity). The difference becomes more pronounced at increasing a_0. Because of the presence of sidelobes, there exist three typical CAS (capture and acceleration scenario) channels when $a_0 \geq 30$ (corresponding to $I > 1 \times 10^{21}\,\mathrm{W/cm^2}$ for $\lambda = 1\,\mu\mathrm{m}$). The energy spread of the outgoing electrons is also discussed in detail.

PACS 41.75.Jv; 42.60.Jf; 42.25.Fx

1 Introduction

With the rapid development of high intensity lasers [1–4], laser acceleration of electrons has received much attention [5–20]. One of the laser acceleration schemes, the capture and acceleration scenario (CAS), was proposed in our previous work [21]. The simulation results are obtained for a standard Gaussian beam (SGB), i.e., TEM_{00} mode Gaussian beam. We found CAS sets in only when the laser field is strong enough ($a_0 \geq 3$, corresponding to intensities $I \geq 1 \times 10^{19}\,\mathrm{W/cm^2}$ at the wavelength of $\lambda = 1\,\mu\mathrm{m}$, where $a_0 = eE_0/m_\mathrm{e}\omega c$ is a dimensionless parameter measuring the laser intensity, E_0 denotes the electric field amplitude of the laser beam at focus, ω the laser circular frequency, e and m_e the electron charge and rest mass, respectively) [22]. The CAS experiment is difficult to carry out not only because the laser intensity should be high enough and the incident electron should be initially relativistic ($\sim 5\,\mathrm{MeV}$), but also the external electron bunch and the laser pulse should meet each other at the laser focus. The recent advances of plasma-based laser acceleration will be helpful for the design of CAS experiment. For a proof-of-principle test where the accelerating fraction is not what concerned us mostly, an electron bunch with a larger radius and wider pulse will be easy to synchronize with the laser pulse spatially and temporally. CAS electrons accelerated to high energy and the electrons not accelerated effectively are separated spatially, which make it feasible to detect the CAS electrons.

We also noticed that to maximize the laser output energy, the radial intensity distribution of an ultrahigh intensity laser beam ends up having a flat-top profile, i.e., a distribution which is nearly uniform over the central region and reduces smoothly to zero away from beam axis [23, 24]. Using three-dimensional (3D) test particle simulations, we confirmed that the CAS is still valid in a focused flattened Gaussian beam (FFGB, FGB is a model describing the flat-topped laser beam) [25, 26]. Electrons injected into such a laser beam with proper initial momentum and incident angle (crossing angle relative to the laser beam direction) can be captured and then violently accelerated. Theoretically, it has been shown when a FGB is focused there are sidelobes around the main focal spot [27, 28]. Experimentally, sidelobes are observed around the main focal spot of a real focused ultra-intense laser beam [3, 4]. The longitudinal electric field of a focused laser beam is separated into several regions by the sidelobes. The sidelobes can influence the optimum (as far as electron acceleration is concerned) CAS electron initial conditions which are important to CAS experiments.

Our simulation results show that the presence of sidelobes influences the optimum initial conditions of electrons for acceleration. For a FFGB with $a_0 \leq 10$ (almost the highest laser intensity achieved so far) the differences of optimum electron initial conditions between FFGB and SGB are negligible. For $a_0 > 10$, the sidelobes should be considered as far as vacuum electron acceleration is concerned. For a FFGB with $a_0 > 30$, there exist three CAS channels: (1) Electrons injected with larger incident angle and are reflected by the sidelobes; (2) Electrons injected with small incident angle and avoiding the sidelobes; (3) Electrons injected with large incident angle and penetrating the sidelobes.

This paper is organized in four sections. In Sect. 2 we describe the FFGB laser field. Simulations and results of laser electron acceleration are presented in Sect. 3. Conclusions are given in Sect. 4.

✉ Fax: +86-21-6564-3815, E-mail: wpx@fudan.edu.cn

2 Laser fields

The laser field adopted here is polarized along the x direction and propagates along the z axis. The electromagnetic field of the laser pulse is described in forms of the vector potential $\boldsymbol{A}$ (A_x, $A_y = 0$, $A_z = 0$). Using the Lorentz gauge, one can obtain the scalar potential by using the equation $\Phi = (c\partial A_x/\partial x)/[\mathrm{i}k - 2\eta/(c\tau)^2]$ where $k = 2\pi/\lambda$ is the laser wave number, $\eta = z - ct$, τ is the pulse duration. Then the electromagnetic field components can be obtained with $\boldsymbol{E} = -\partial\boldsymbol{A}/\partial t - \nabla\Phi$ and $\boldsymbol{B} = \nabla \times \boldsymbol{A}$ as in [25]. Since the wave equations for vector potential and electric field have the same form, following the method introduced in [25–29], instead of the electric field, we set A_x of a FFGB as [26]

$$
\begin{aligned}
A_x =& A_0 \frac{w_N(0)}{w_N(z)} \exp\left(-\frac{r^2}{w_N^2(z)}\right) \\
&\times \exp\left\{\mathrm{i}\left[-\varphi_N(z) - \varphi_0 + \frac{kr^2}{2R_N(z)}\right]\right\} \\
&\times \sum_{n=0}^{N} c_n^{(N)} L_n\left(\frac{2r^2}{w_N^2(z)}\right) \\
&\times \exp\left[-2in\varphi_N(z)\right] f(\eta) \exp(ik\eta) \ , \qquad (1)
\end{aligned}
$$

in which the form factor of the laser pulse is assumed as $f(\eta) = \exp[-((z-ct)/c\tau)^2]$, L_n is the nth Laguerre polynomial, and the $c_n^{(N)}$ coefficient is defined as

$$
c_n^{(N)} = (-1)^n \sum_{m=n}^{N} \binom{m}{n} \frac{1}{2^m} \ ,
$$

where $\binom{m}{n}$ denotes the binomial coefficient. The parameters $w_N(z)$, $R_N(z)$ and $\varphi_N(z)$ are given by $w_N(z) = |A| w_N(0)(1+G^2)^{1/2}$, $R_N(z) = AB\frac{1+G^{-2}}{1+BC(1+G^{-2})}$ and $\varphi_N(z) = \tan^{-1} G$, where $G = \frac{B}{A}\frac{2}{kw_N^2(0)}$, A, B and C are the elements of the pertaining $ABCD$ matrix given by the product of the matrices corresponding to the focusing mirror and free propagation. Furthermore, $w_N(0) = w_0/\sqrt{N+1}$, w_0 is waist size of the FGB, and φ_0 is the laser initial phase.

The extension of the area in which the laser field amplitude is approximately uniform is governed by the integer parameter N. The beam is Gaussian for $N = 0$, the top of the distribution curve becomes more and more flattened in the waist plane as N increases. When $N \to \infty$, the curve becomes a rect function [rect(r) is defined as 1 if $|r| < 1$ but 0 elsewhere] in the waist plane or a circ function (defined as the Fourier transform of rect function) in the focal plane. Figure 1 shows the amplitude profiles of E_x and E_z in the focal plane for FFGB and SGB, where $w'0 \approx (\lambda f)/(\pi w_f)$ represents the laser beam width at focus, f is the focal length, w_f is the spot size at the focusing mirror. In our case, without loss of generality, we let $w_f = w_0$. Figure 1a and c are for $|E_x|$ and $|E_z|$ of SGB in focal plane. Figure 1b and Fig. 1d are for those of FFGB. The upper inserts show the electric field amplitudes as functions of x along line $y = z = 0$. Please notice that, when $N > 0$ there are sidelobes outside the main focal spot because of diffraction.

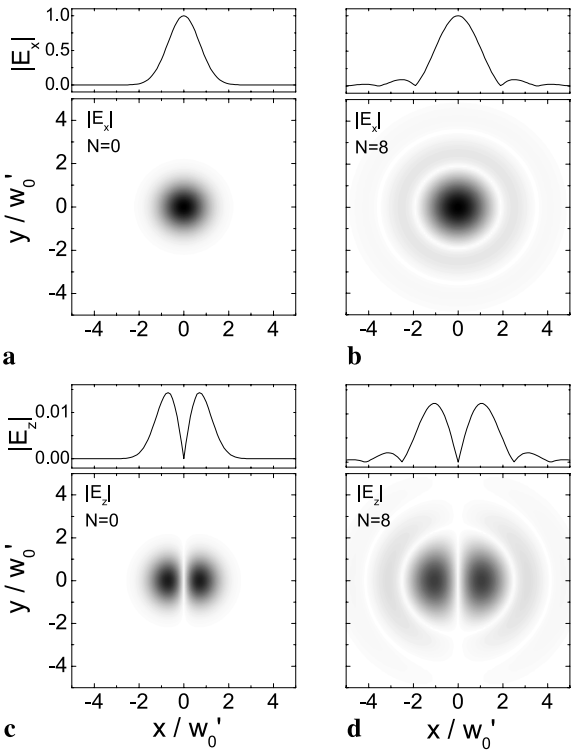

FIGURE 1 Amplitude profiles of E_x and E_z in the focal plane for FFGB ($N = 8$, a beam with a flat-topped intensity distribution before focusing) and SGB ($N = 0$). Laser intensity $a_0 = 1$

3 Simulation model and results

Throughout this paper the momentum, length and time are normalized by $m_e c$, k and ω, respectively. Other parameters are kept constant: laser beam width at focus $w_0' = 60$ and laser pulse duration $\tau = 500$.

To study the characteristics of electron acceleration by the SGB and FFGB propagating in vacuum, the relativistic Newton–Lorentz equation [21, 22] $\mathrm{d}\boldsymbol{P}/\mathrm{d}t = -e(\boldsymbol{E} + \boldsymbol{v} \times \boldsymbol{B})$ (where $\boldsymbol{v}$ is the electron velocity in units of c, $\boldsymbol{P} = \gamma\boldsymbol{v}$ is the electron momentum, and $\gamma = (1 - v^2)^{-1/2}$ is the Lorentz factor) is solved using 3D test particle simulation.

The single-particle simulations are carried out to show the difference between laser beams with different N and a_0. Electrons with initial momentum P_0 are injected in the $x - z$ plane, towards the coordinate origin, at a crossing angle θ with respect to the laser beam. Without the influence of laser field, the electrons will arrive at the original point when the laser pulse center arrives at the original point (time delay between laser pulse and electron $\Delta t = 0$). The laser initial phase φ_0 (denoting the phase of an electron with respect to the carrier wave since Δt is fixed) is scanned from 0 to 2π. The single-particle simulation is not the real case of electron bunch interacting with laser beam, but it shows the main physical characteristics more clearly.

To be effectively accelerated, the electrons have to pass through the sidelobes to enter the high intensity laser field region. The threshold transverse momentum P_{xc} for electrons to pass through the potential barrier of the side-lobe can be expressed as [30]

$$P_{xc} = (a_0 \xi_N)/\sqrt{2}\,, \tag{2}$$

which is predicted by the ponderomotive potential $V_{\text{pond}} = (\sqrt{1+|\boldsymbol{A}|^2/2}-1)m_e c^2$, and ξ_N represents the ratio of the peak intensity of the side-lobe to a_0 [31, 32]. Since P_{xc} is proportional to laser intensity, the effects of sidelobes on vacuum electron acceleration will be more notable as increasing a_0.

Since the electron final energy γ is sensitive to the laser initial phase φ_0 as well as the electron initial momentum P_0 and incident angle θ, the distributions of electron final energy γ_{av} presented in Fig. 2 is the value averaged over the range of $\varphi_0 \in [0, 2\pi]$. These distributions of outgoing energy are displayed in a two-dimensional space spanned by P_0 and θ. For SGB (without sidelobes), there is one continuous $P_0 - \theta$ region within which electrons can be effectively accelerated. The differences of optimum electron initial conditions between FFGB and SGB are negligible when $a_0 = 10$, and differences become evident as a_0 increases. For the FFGB with $a_0 \geq 30$, the $P_0 - \theta$ region for effective acceleration is divided into two parts by a dashed line, which indicates the threshold transverse momentum P_{xc} for electrons to pass through the potential barrier of the side-lobe [30]. When the initial transverse momentum P_{xi} is larger than P_{xc}, electrons can go through the side-lobe and be effectively accelerated. When $P_{xi} < P_{xc}$, electrons with a small incident angle θ can pass within a lower side-lobe and then can also enter the intense field region and be accelerated. When the laser intensity $a_0 \geq 30$, the side-lobe is so strong ($\sim a_0/10$ for $N = 8$) that it can also capture and accelerate electrons [22].

As an example, we take $a_0 = 80$ to study the characteristics of electron dynamics in the high-intensity FFGB laser field. Results show that there exist three typical CAS electron trajectories (as shown in Fig. 3). When $P_{xi} > P_{xc}$ ($P_0 \sim 32$ and $\tan\theta \sim 0.24$), the electrons can pass through the sidelobes and enter the high intensity region of E_z. While for $P_{xi} < P_{xc}$, when θ is small ($P_0 \sim 32$ and $\tan\theta \sim 0.07$), the electrons bypass the intense side-lobe and are then accelerated to high energies; when θ is large ($P_0 \sim 9$ and $\tan\theta \sim 0.2$), the electrons are reflected by the side-lobe. Although the side-lobe can accelerate electrons too, this is not the case we are looking

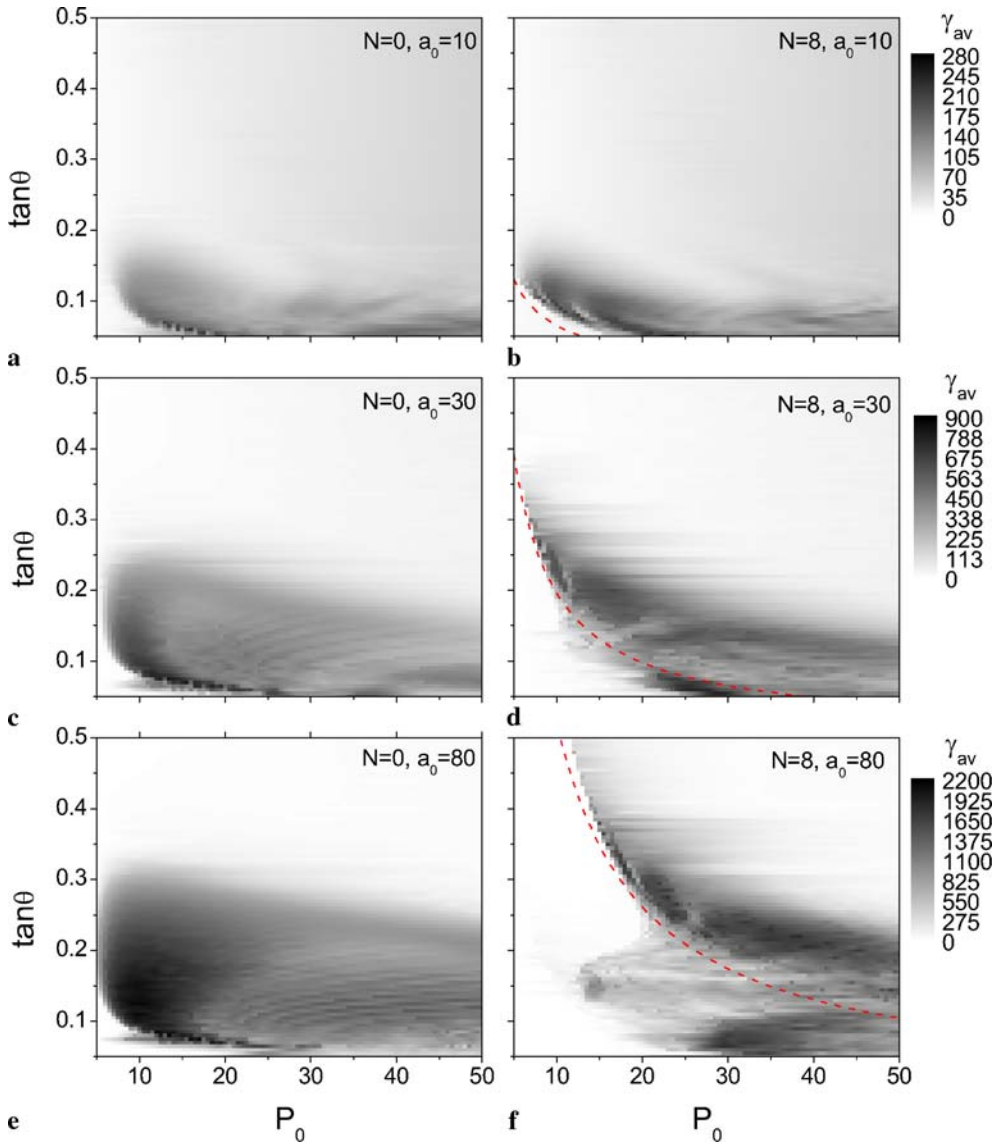

FIGURE 2 The distributions of electron final energy γ_{av} (γ_{av} is averaged in the range of $\varphi_0 \in [0, 2\pi]$) in the two-dimension space constructed by the electron initial momentum P_0 and the incident angle θ. (**a**) $N = 0$, $a_0 = 10$, (**b**) $N = 8$, $a_0 = 10$, (**c**) $N = 0$, $a_0 = 30$, (**d**) $N = 8$, $a_0 = 30$, (**e**) $N = 0$, $a_0 = 80$ and (**f**) $N = 8$, $a_0 = 80$. Other parameters are $w_0' = 60$ and $\tau = 500$. *Dashed lines* represents $P_{xi} = P_{xc}$

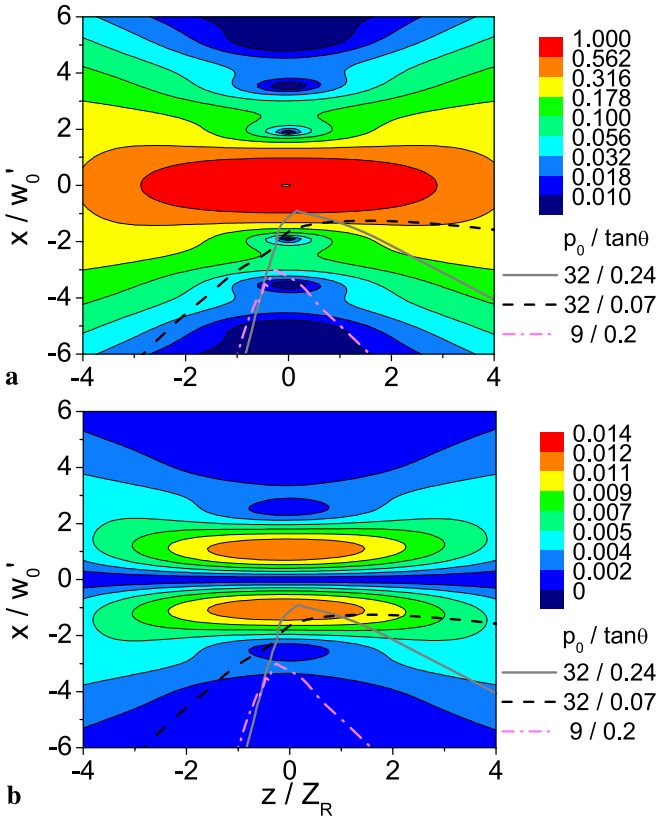

FIGURE 3 Intensity distribution of (**a**) E_x and (**b**) E_z of FFGB ($N = 8$) in $x-z$ plane. Electron trajectories for initial conditions ($P_0 = 32$, $\tan\theta = 0.24$, *solid lines*), ($P_0 = 32$, $\tan\theta = 0.07$, *dashed lines*) and ($P_0 = 9$, $\tan\theta = 0.2$, *dash-dotted lines*) are shown also. Other parameters are $a_0 = 80$, $w_0' = 60$ and $\tau = 500$

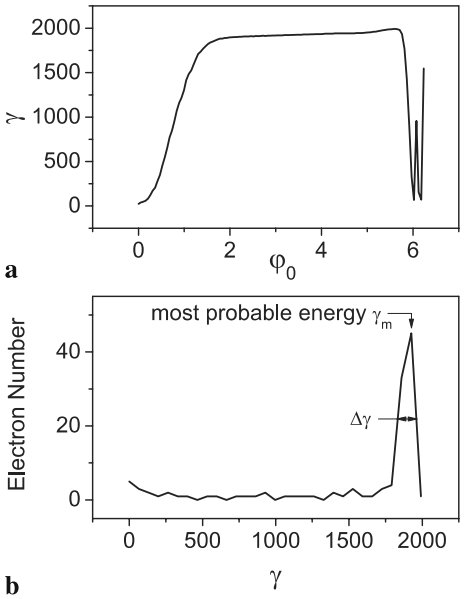

FIGURE 4 Illustration of relative energy spread $\Delta\gamma/\gamma_m$ for electrons with initial phase $\varphi_0 \in [0, 2\pi]$. (**a**) the electron final energy as a function of φ_0 and (**b**) the corresponding spectrum of (**a**). Electron initial momentum $P_0 = 32$ and incident angle $\tan\theta = 0.24$. Other parameters are $a_0 = 80$, $w_0' = 60$ and $\tau = 500$

for since the electron final energy is very low due to the low intensity of E_z inside the side-lobe.

It has long been known that for the case of plane E-M wave in vacuum, the correlation between the outgoing energy and the scattering angle of accelerated electrons can be described by a single-valued function [33–38]. However, for a focused laser beam in vacuum, we get that electrons even with the same outgoing energy will have an angular spread [39]. Namely, the energy spread in vacuum acceleration by a focused laser beam is inherent and can not be avoided in any vacuum laser acceleration experiment. But, according to our simulation results, this energy spread is much smaller than that induced by different initial conditions of different electrons in a bunch. To evaluate the characteristics of the electron energy spread in FFGB with different initial conditions, we calculated the relative energy spread $\Delta\gamma/\gamma_m$, where γ_m is the most probable energy and $\Delta\gamma$ the full width at half maximum of the electron energy spectrum. Figure 4 is a scheme for the treatment of these data, where electrons with initial momentum P_0 are injected towards the coordinate origin with $\Delta t = 0$, and φ_0 is scanned from 0 to 2π, as explained earlier. Figure 4a shows the electron output energy γ as a function of φ_0 and Fig. 4b shows the energy spectrum of these electrons. Following this way, we scan for different initial momentum and injected angle. The simulation results are shown in Fig. 5, where a and b are the relative energy spread and most probable energy for $N = 0$, c and d, e and f are for $N = 4$ and $N = 8$, respectively. We note that the case a little fraction of electrons with $\varphi_0 \in [0, 2\pi]$ is accelerated to high energy and the average energy γ_{av} is high which is shown in Fig. 2 is excluded from Fig. 5. A good acceleration channel should be one with high outgoing energy, high acceleration efficiency and low energy spread. From Figs. 5 and 2, we can choose the favorite electron initial conditions according to the most concerned factors.

It is known that the laser pulse shape (the degree to which it is flat-topped) will fluctuate from pulse to pulse (pulse jitter). From Fig. 5c–f we see that the accelerating region of initial conditions around $P_0 \sim 32$ and $\tan\theta \sim 0.24$ are not very sensitive, and it makes little difference between $N = 4$ and $N = 8$. The trajectories of electrons injected at the same momentum and angle for both $N = 4$ and $N = 8$ are shown in Fig. 6, where color presents the electron energy γ. The propagating directions of accelerated electrons are close, both for electrons with different φ_0 in the same FFGB and for electrons in $N = 4$ and $N = 8$ laser beams. As far as the initial conditions and outgoing direction are concerned, the electron acceleration through channel around $P_0 \sim 32$ and $\tan\theta \sim 0.24$ is not very sensitive to the pulse jitter, while the channel with small incident angle is contrary.

The single-particle simulations mentioned above show the main physical characteristics clearly, especially when comparing with different pulse shape, laser intensity, etc. When the laser intensity is strong enough, there exist three CAS channels in the FFGB field. The acceleration of electrons with initial transverse momentum larger than the threshold transverse momentum is not very sensitive to initial conditions, and yields a small energy spread. However, when an electron bunch with bunch length comparable or larger than the laser pulse width is concerned, it may be more complex. The bunch is so large that some of the electrons will experience a lower laser field. This will surely influence the output bunch prop-

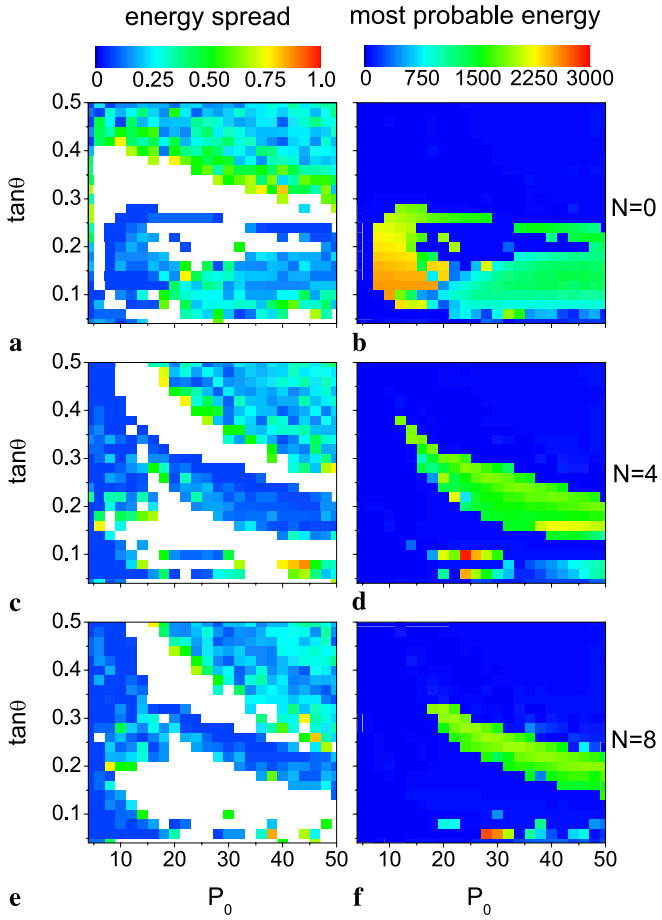

FIGURE 5 The distributions of relative energy spread $\Delta\gamma/\gamma_m$ and most probable energy for electrons with initial phase $\varphi_0 \in [0, 2\pi]$ in the two-dimension space constructed by the electron initial momentum P_0 and the incident angle θ. (**a**) and (**b**) $N = 0$, (**c**) and (**d**) $N = 4$, (**e**) and (**f**) $N = 8$. Other parameters are $a_0 = 80$, $w_0' = 60$ and $\tau = 500$

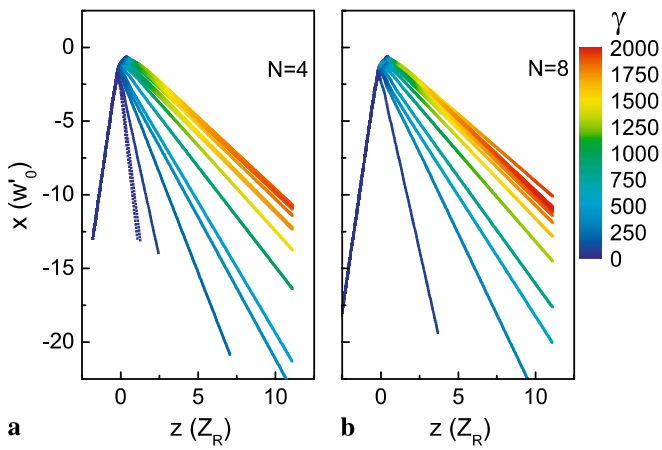

FIGURE 6 Trajectories of electrons with initial phase $\varphi_0 \in [0, 2\pi]$ in $N = 4$ (**a**) and $N = 8$ (**b**) FFGB, where color shows the electron energy γ

erties. In the following the characteristics of electron bunches driven by FFGB within the three channels found in single-particle simulations are studied. The schematic geometry of electron bunch captured and accelerated by a laser beam is shown in Fig. 7. Injected electrons are uniformly distributed with radius $r = 2w_0'$ and length $L = 2000$. Without the influence of laser field, the electron bunch center will arrive simultaneously with the laser pulse center arrives at the coordinate center. Electrons with different Δt will experience different parts of the laser phase. When the laser pulse width or the electron bunch length is much larger than the laser wavelength, the influence of φ_0 is not significant. Without loss of generality, the laser initial phase φ_0 is set to 0. The crossing angle α between electron spectrometer and laser beam is optimized to get the highest averaged electron final energy for given initial conditions. The collecting angle β of the electron spectrometer is set to be 2°.

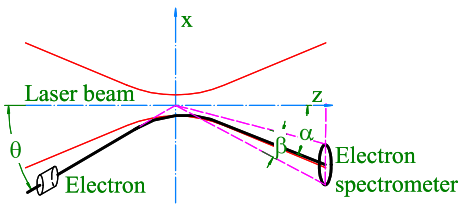

FIGURE 7 Schematic geometry of electrons captured and accelerated by a laser beam. Injected electrons are uniformly distributed with radius $r = 2w_0'$ and length $L = 2000$. The crossing angle between electron spectrometer and laser beam α is optimized for different initial conditions. Electron collecting angle $\beta = 2°$

Electron bunches accelerated by FFGB with $N = 8$ and $a_0 = 80$ through three channels are simulated and the results are shown in Fig. 8. Figure 8a, c and e are the angular spreads of output electrons in the $x - y$ plane, where points denote electrons, color of points shows the energy of electrons, and solid circles show the collecting aperture of electron spectrometer (as shown in Fig. 7). Figure 8b, d and f present the spectra of electrons collected by the spectrometer corresponding to Fig. 8a, c and e, respectively. Because the dimension of the electron bunch is larger than that of the laser pulse, some marginal electrons experience quite a weak laser field and go almost straightforward. Electrons experiencing a stronger laser field (but weaker than the CAS laser intensity threshold [22]) are reflected by the field. Electrons near the bunch center experience a laser field with intensity higher than the CAS laser intensity threshold and are captured and accelerated effectively (a few of these central electrons with unsuitable Δt can not be captured and will be scattered out of the laser beam [22]). CAS electrons accelerated to high energy and the scattered or the straightforward electrons not accelerated effectively are separated spatially, which make it feasible to experimentally detect the CAS electrons. For the case of Fig. 8a and b ($P_0 = 32$, $\tan\theta = 0.24$), the electron capture fraction is low, but the incident angle is so large that the electrons will never meet the brim of the focusing mirror of the laser beam, which may simplify the design of a CAS experiment. For the case of Fig. 8c and d ($P_0 = 32$, $\tan\theta = 0.07$), the electron capture fraction is high (close to the optimum case of SGB), and the maximum final energy is higher than that in other cases. The case of Fig. 8e and f ($P_0 = 9$, $\tan\theta = 0.2$) is not that wanted due to the low capture fraction and low output energy.

When a focused SGB is adopted, the incident angle of CAS channel is small. A tiny hole should be punched on the focusing mirror to let the electrons through, or, an external magnetic field is required to let the electrons bypass the mirror. These will influence the laser field or

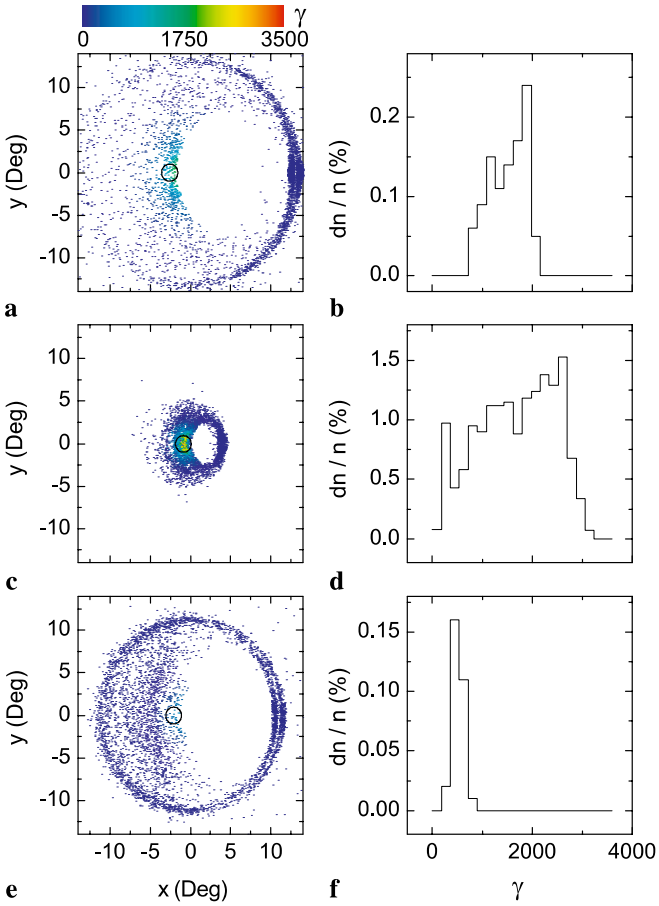

FIGURE 8 Angular distributions of output electrons in $x-y$ plane [(**a**) for ($P_0 = 32$, $\tan\theta = 0.24$), (**c**) for ($P_0 = 32$, $\tan\theta = 0.07$) and (**e**) for ($P_0 = 9$, $\tan\theta = 0.2$)], where *points* denotes electrons, *color of points* shows the energy of electrons, and *solid circles* show the collecting aperture of electron spectrometer. (**b**), (**d**) and (**f**) present the spectra of collected electrons corresponding to (**a**), (**c**) and (**e**), respectively. Schematic geometry of electron injection and collection is shown in Fig. 4. Other parameters are $a_0 = 80$, $w_0' = 60$ and $\tau = 500$

make the CAS experiment difficult to carry out. Using a focused FGB with diffraction rings may overcome this difficulty because the big incident angle of CAS channel can make the incident electron enter the laser field without meeting the focusing mirror. These results can shed some light on the experimental design to test the CAS scheme.

4 Conclusion and discussion

In conclusion, the presence of sidelobes in focused flat-top laser beams influences the electron initial conditions (optimum initial momentum) required for effective CAS. When the laser intensity is low ($a_0 \leq 10$ for $N = 8$), the difference of optimum electron initial conditions between FFGB and SGB is negligible. This difference becomes, however, evident with increasing a_0, and the sidelobes should be considered as far as CAS electron acceleration is concerned. When the laser intensity is strong enough ($a_0 \geq 30$ for $N = 8$), there exist three CAS channels in the FFGB field. Electrons with initial transverse momentum larger than the threshold transverse momentum needed to pass through the ponderomotive potential barrier of the sidelobes have a large incident angle. Electrons with small incident angle have a high rate of being captured, and the maximum output energy is higher than that of SGB. These results may be helpful for the design of a CAS experiment. Here we would like to point out that it may be too early to compare vacuum laser acceleration scheme with plasma-based laser acceleration such as LWFA, etc. presently, because these two kinds of laser acceleration schemes are in totally different R&D (research and development) status. More experimental and theoretical works are needed before we can say something about if the CAS scheme is competitive with other schemes.

ACKNOWLEDGEMENTS The authors would like to thank S.Z. Fu, X.L. Xie and L. Xia for helpful discussions. This work is supported partly by National Natural Science Foundation of China under Contracts No.10475018 and No.10335030.

REFERENCES

1 M. Aoyama, K. Yamakawa, Y. Akahane, J. Ma, N. Inoue, H. Ueda, H. Kiriyama, Opt. Lett. **28**, 1594 (2003)
2 S. Witte, R.T. Zinkstok, W. Hogervorst, K.S.E. Eikema, Opt. Express **13**, 4903 (2005)
3 S.-W. Bahk, P. Rousseau, T.A. Planchon, V. Chvykov, G. Kalintchenko, A. Maksimchuk, G.A. Mourou, V. Yanovsky, Opt. Lett. **29**, 2837 (2004)
4 L.Q. Liu, H.S. Peng, K.N. Zhou, X.D. Wang, X. Wang, X.M. Zhang, Q.H. Zhu, X.J. Huang, X.F. Wei, R. Huan, Proc. SPIE **5856**, 646 (2005)
5 T. Tajima, G. Mourou, Phys. Rev. ST Accel. Beams **5**, 031 301 (2002)
6 W.P. Leemans, B. Nagler, A.J. Gonsalves, Cs. Tóth, K. Nakamura, C.G.R. Geddes, E. Esarey, C.B. Schroeder, S.M. Hooker, Nat. Phys. **2**, 696 (2006)
7 S.P.D. Mangles, C.D. Murphy, Z. Najmudin, A.G.R. Thomas, J.L. Collier, A.E. Dangor, E.J. Divall, P.S. Foster, J.G. Gallacher, C.J. Hooker, D.A. Jaroszynski, A.J. Langley, W.B. Mori, P.A. Norreys, F.S. Tsung, R. Viskup, B.R. Walton, K. Krushelnick, Nature **431**, 535 (2004)
8 C.G.R. Geddes, Cs. Tóth, J. van Tilborg, E. Esarey, C.B. Schroeder, D. Bruhwiler, C. Nieter, J. Cary, W.P. Leemans, Nature **431**, 538 (2004)
9 J. Faure, Y. Glinec, A. Pukhov, S. Kiselev, S. Gordienko, E. Lefebvre, J.P. Rousseau, F. Burgy, V. Malka, Nature **431**, 541 (2004)
10 Y.I. Salamin, C.H. Keitel, Phys. Rev. Lett. **88**, 095 005 (2002)
11 Y.I. Salamin, C.H. Keitel, Appl. Phys. Lett. **77**, 1082 (2000)
12 Y.I. Salamin, Phys. Lett. A **335**, 289 (2005)
13 W. Yu, V. Bychenkov, Y. Sentoku, M.Y. Yu, Z.M. Sheng, K. Mima, Phys. Rev. Lett. **85**, 570 (2000)
14 W. Yu, Z.Y. Chen, M.Y. Yu, L.J. Qian, P.X. Lu, R.X. Li, K. Koyama, Phys. Rev. E **66**, 036 406 (2002)
15 H. Liu, X.T. He, H. Hora, Appl. Phys. B **82**, 93 (2006)
16 C. Varin, M. Piché, Appl. Phys. B **74**, 83 (2002)
17 D. Li, K. Imasaki, Appl. Phys. Lett. **86**, 031 110 (2005)
18 K.P. Singh, Appl. Phys. Lett. **87**, 254 102 (2005)
19 Q. Kong, S. Miyazaki, S. Kawata, K. Miyauchi, K. Sakai, Y.K. Ho, K. Nakajima, N. Miyanaga, J. Limpouch, A.A. Andreev, Phys. Rev. E **69**, 056 502 (2004)
20 D.N. Gupta, H. Suk, Phys. Plasmas **13**, 013 105 (2006)
21 P.X. Wang, Y.K. Ho, X.Q. Yuan, Q. Kong, N. Cao, A.M. Sessler, E. Esarey, Y. Nishida, Appl. Phys. Lett. **78**, 2253 (2001)
22 J. Pang, Y.K. Ho, N. Cao, L. Shao, Y.J. Xie, Z. Chen, S.Y. Zhang, Appl. Phys. B **76**, 617 (2003)
23 S. De Silvestri, P. Laporta, V. Magni, O. Svelto, B. Majocchi, Opt. Lett. **13**, 201 (1988)
24 F G. Patterson, R. Gonzales, M.D. Perry, Opt. Lett. **16**, 1107 (1991)
25 W. Wang, P.X. Wang, Y.K. Ho, Q. Kong, Z. Chen, Y. Gu, S.J. Wang, Europhys. Lett. **73**, 211 (2006)
26 F. Gori, Opt. Commun. **107**, 335 (1994)
27 V. Bagini, R. Borghi, F. Gori, A.M. Pacileo, M. Santarsiero, D. Ambrosini, G. Schirripa, J. Opt. Soc. Am. A **13**, 1385 (1996)
28 M. Santarsiero, D. Aiello, R. Borghi, S. Vicalvi, J. Mod. Opt. **44**, 633 (1997)
29 P.X. Wang, J.X. Wang, Appl. Phys. Lett. **81**, 4473 (2002)

30 Y.K. Ho, J.X. Wang, L. Feng, W. Scheid, H. Hora, Phys. Lett. A **220**, 189 (1996)
31 T.W.B. Kibble, Phys. Rev. Lett. **23**, 1054 (1966)
32 T.W.B. Kibble, Phys. Rev. **150**, 1060 (1966)
33 F.V. Hartemann, S.N. Fochs, G.P. Le Sage, N.C. Luhmann, J.G. Woodworth, M.D. Perry, Y.J. Chen, A.K. Kerman, Phys. Rev. E **51**, 4833 (1995)
34 F.V. Hartemann, A.L. Troha, N.C. Luhmann, Z. Toffano, Phys. Rev. E **54**, 2956 (1996)
35 M.V. Fedorov, S.P. Goreslavsky, V.S. Letokhov, Phys. Rev. E **55**, 1015 (1996)
36 Y.I. Salamin, F.H.M. Faisal, Phys. Rev. A **55**, 3678 (1997)
37 F.V. Hartemann, J.R. Van Meter, A.L. Troha, E.C. Landahl, N.C. Luhmann, H.A. Baldis, A. Gupta, A.K. Kerman, Phys. Rev. E **58**, 5001 (1998)
38 F.V. Hartemann, A.K. Kerman, Phys. Rev. Lett. **76**, 624 (2001)
39 Z. Chen, Y.K. Ho, Y.J. Xie, S.Y. Zhang, Z. Yan, J.J. Xu, Y.Z. Lin, J.F. Hua, Appl. Phys. Lett. **85**, 2475 (2004)